nature communications

Article

https://doi.org/10.1038/s41467-026-75355-4

# Key link between iron and the size structure of three major mesoplanktonic groups in the upper ocean

Received: 29 June 2025

Accepted: 29 June 2026

Published online: 14 July 2026

Check for updates

Mathilde Dugenne[1] ✉, Marco Corrales-Ugalde[2], Jessica Y. Luo[3], Lars Stemmann[1], Jean-Olivier Irisson[1], Fabien Lombard[1], Todd O'Brien[4], Charles Stock[3], PSSdb data contributors* & Rainer Kiko[5] ✉

In marine ecosystems, critical services like fish production, carbon export, or the delivery of nutrients through $N_2$-fixation rely heavily on the size spectrum of pelagic organisms, particularly mesoplankton (200-20,000 μm). However, the linkages between environmental factors and mesoplankton spectral biogeography remain largely unresolved, as so far only limited datasets exist to understand the large-scale shifts in mesoplankton size. Using global compilations of Rhizarian, colonial $N_2$-fixer, and Crustacean images, we reveal the role of iron in shaping the size structure and related biogeography of these groups. Our findings underscore the importance of atmospheric sources of iron for $N_2$-fixers and Rhizarians while total iron, accounting for organic and inorganic compounds, appeared to explain a high percentage of the variance in Crustacean size structure via apparent recycling. Using environmental explanatory variables, our models reached high $R^2$ (0.93, 0.88, and 0.79 respectively), providing robust predictions of mesoplankton size structure related to elemental cycling and ecosystem services. Our results suggest that without compensatory mechanisms, future increases in global temperatures could have negative effects on mesoplankton size, possibly limiting carbon export from the productive layers to sequestration depth, that might be offset by expected increases in iron inputs that benefit $N_2$-fixers, Rhizarians, and eventually Crustaceans.

The decrease of organism abundances in increasing size classes is a universal feature of both terrestrial and aquatic ecosystems[1–4] that relates to ecosystem functioning and services like carbon export and fish biomass production for the latter[5–8]. Both services are affected by size-dependent processes, such as $CO_2$ uptake[9] and respiration[10], predation[11], organic matter packaging[12,13] and passive sinking[14], that underpin all links of marine food webs, from bacteria to whales[15–17]. As a result, changes affecting plankton communities are currently observed through the lens of the size spectrum framework via three parameters[18]: the spectral intercept (which will increase or decrease if all plankton groups are equally affected), the slope (which will vary with differences in transfer efficiency), and the linearity (which may decrease under perturbations that alter only certain size classes). Using this framework, ecologists have shown that most plankton communities varied in size with latitudinal gradients[19,20], following the set of empirical rules and theoretical principles linking global

[1]Laboratoire d'Océanographie de Villefranche, CNRS, Sorbonne Université, Villefranche-sur-mer, France. [2]Atmospheric and Oceanic Sciences, Princeton University, Princeton, NJ, USA. [3]NOAA/OAR Geophysical Fluid Dynamics Laboratory, Princeton, NJ, USA. [4]NOAA Fisheries - Office of Science and Technology, Silver Spring, MD, USA. [5]GEOMAR Helmholtz Centre for Ocean Research Kiel, Kiel, Germany.*A list of authors and their affiliations appears at the end of the paper. ✉e-mail: mdugenne@hotmail.com; rkiko@geomar.de

environmental gradients to plankton size structure, here defined as spectral biogeography, reviewed by Barton et al.[21]. In their review, the authors identified seasonal and latitudinal variations of temperature and oxygen levels, resource availability and prey size structure, as well as ocean circulation as major structuring elements of the pelagic realm. Yet in practice, their effects are often hard to disentangle as most factors co-vary in marine ecosystems and some relationships appear contradictory to explain the spectral biogeography of the three groups that dominate mesoplankton communities in the upper ocean[22]: heterotrophic Crustaceans, mixotrophic Rhizarians, and autotrophic $N_2$-fixers represented by the genus *Trichodesmium*. For example, Crustacean body size decreases under high temperature and low oxygen levels, a relationship known as the Temperature-Size Rule[23], but also surprisingly with phytoplankton productivity and cell size[24]. Opportunist mixotrophs are equally unpredictable, as they should be favored in oligotrophic ecosystems, where sources of inorganic and organic nutrients are scarce, and paradoxically in productive systems that undergo large seasonal fluctuations in resource availability[21]. Lastly, future projections of marine $N_2$-fixation are still difficult despite its importance in delivering new nutrients to oligotrophic ecosystems[25], as greater temperatures should increase the growth of large $N_2$-fixers like *Trichodesmium*, but also limit the supply of their essential nutrients that would require a lower surface:volume ratio. Overall, previous meta-analysis presenting the biogeography of Crustacean copepod[24], mixotrophic[26], and heterotrophic Rhizarians[27], and colonial $N_2$-fixers[19] only explained up to 50% of the variance in mesoplankton occurrences or sizes, leaving important sources of variability unexplained that the authors often linked to missing explanatory variables or to further clustering within broad groups. Eventually, all relationships linking environmental factors to organism size spectra remain largely enigmatic, in part due to the paucity of direct size structure compilations and related environmental gradients, and to additional traits (diet, morphotypes) underpinning specific adaptations within broader phyla.

In recent years, the size-structure framework has been used in conjunction with other traits (e.g., feeding strategy, migration, buoyancy) to represent plankton communities along a few functional axes, instead of numerous taxa that cannot all be monitored or cultivated[28–35]. To do so, ecologists have been using new imaging devices that provide high-throughput proxies of functional complexity across the five orders of magnitude in plankton sizes[36,37]. Here, we present a compilation of keystone mesoplankton groups' size spectra measured from imaging devices deployed globally between 0 and 200 m. We depict the spectral biogeography of Crustaceans based on net-collected samples imaged with benchtop scanners, as well as colonial $N_2$-fixers and Rhizarians using Underwater Vision Profilers (UVPs), since these organisms are severely damaged by nets. We first explore the relationships between their size distributions and environmental descriptors (e.g., temperature, resource availability, or mesoscale circulation), including diverse iron supply proxies, before searching for specific adaptations to environmental factors within these broad groups. Ultimately, we aim at improving our mechanistic understanding of marine ecosystem functioning under diverse stressors, as we used the linkages between size structure and environmental gradients in conjunction with machine learning models (i.e., boosted regression trees) to generate global predictions of group-specific size structure. These will help refine or validate plankton models, with the goal to constrain the future projections of ecosystem processes under climate change.

## Results

### A spectral analysis of three keystone mesoplankton biogeography in the upper ocean

In this study, we compiled images from benchtop scanners and UVP that have been regularly deployed in all major ocean basins since the mid 2000s, with the highest concentration of samples recorded within the epipelagic layer of the subtropics (Fig. 1a, b). Despite their relative spatial proximity, regions with the strongest sampling bias were typically sampled months apart (Fig. 1c–f), providing discontinuous records of mesoplankton size spectrum in space and time that helped us disentangle the effect of seasonal or decadal trends from broad spatial gradients on their spectral biogeography. After taxonomic standardization, all image annotations pointed to the global importance of colonial $N_2$-fixers, Rhizarians, and Crustaceans within mesoplankton communities, as the first two groups represented 45% and 15% of the total images compiled from UVP datasets, while the latter corresponded to 81% of the overall scanner images aligning with the known bias for non-gelatinous taxa collected with traditional nets (Fig. 1g, h). We combined UVP profiles and scanned nets to compute the epipelagic size spectra of colonial $N_2$-fixers (exclusively represented by two morphotypes of the colonial genus *Trichodesmium*), Rhizarians (regrouping the 4 main classes of Acantharia, Collodaria, Foraminifera, and Phaeodaria), and Crustaceans (including three classes of Copepoda, Malacostraca, and Ostracoda), averaged by 1° latitude, longitude, and by year-month bins to limit statistical bias arising from autocorrelated measurements. Important similarities across the three main groups' size spectra can be seen in the global compilation (Fig. 2a), as they all show a log-linear decline in abundance with increasing size classes following slopes close to the canonical value of −1 (Supplementary Fig. 1). Yet, their total abundances, obtained by integrating individual size spectra across all observed sizes, span four orders of magnitude, ranging between ~0.1 and ~1000 particles $m^{-3}$. This represents a significant spatio-temporal variability across the datasets, particularly for colonial $N_2$-fixers, which present the highest percentage of empty records, with 64% of the spatio-temporal bins without occurrences (Fig. 2b), compared to Rhizarians (36%) and Crustaceans (12%).

We found that colonial $N_2$-fixers were largely restricted to the subtropical latitudes, between −20 and 20 °N, similarly to Rhizarians, though they were also relatively abundant at higher latitudes and in the Californian upwelling system (Fig. 2c).

In comparison, Crustaceans were generally ubiquitous, with the highest abundances observed in productive ecosystems (e.g., polar, upwelling, and coastal regions). Caution should be taken when using or interpreting the few observations located in the Southern Ocean, but our results shed light on previously undersampled regions that could be potential hotspots for marine mesoplankton, as reflected in other parts of the globe where environmental conditions are highly similar (Arctic Ocean, upwellings, etc.).

### Iron, a key descriptor of mesoplankton spectral biogeography in the upper ocean

Boosted regression tree models fitted to PSSdb records (response variable) and global datasets of environmental descriptors (explanatory variables) yielded global predictions that match the magnitude and variability of total abundances derived from spectral parameters (Fig. 2c) with relatively high $R^2$ (0.93, 0.88, and 0.79 for $N_2$-fixers, Rhizarians, and Crustaceans, respectively, Table 1). Bootstrapped model predictions were generally more variable in regions of peak abundances with fewer PSSdb observations, reflecting larger uncertainties in subpolar and polar ecosystems, for all three mesoplankton groups, with the highest coefficient of variations ranging between 60 and 120% on average (Supplementary Fig. 2).

The main bottom-up factors explaining the spectral biogeography of Crustaceans, Rhizarians, and colonial $N_2$-fixers, indicated by their respective ranks in terms of their gradual importance in the model variance explained, typically included temperature as well as diverse iron proxies (Table 1).

Our full model included several proxies linked to different, but not mutually exclusive, pools of iron to reflect the diversity in natural

https://doi.org/10.1038/s41467-026-75355-4

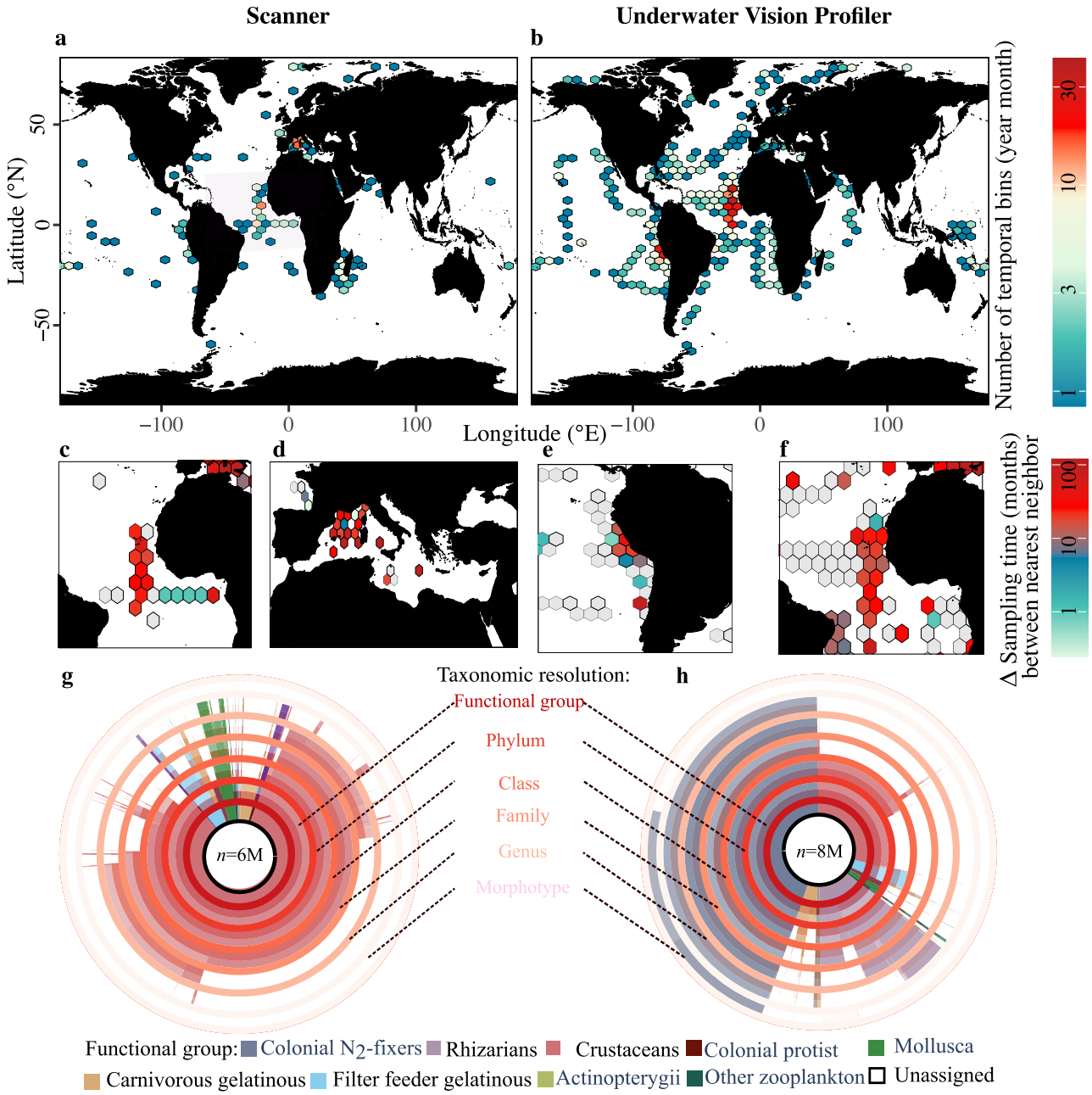


**Fig. 1 | Resolution and diversity in taxonomic annotations of the Scanner (left) and Underwater Vision Profiler (UVP, right) imaging datasets.** Spatial coverage of the scanner (**a**) and UVP (**b**) datasets produced in the Pelagic Size Structure database. The colors represent the number of temporal (year-month) bins in these datasets. Each spatial bin has been sampled irregularly over time, often months apart in the most biased regions of the tropical Atlantic (**c**, **f**), Mediterranean Sea (**d**), or eastern Equatorial Pacific (**e**). Hence, our datasets represent a unique opportunity to study how mesoplankton size structure fluctuates in space and time because of environmental variables. Diversity of taxonomic annotations (*n* represents the total number of images in each dataset) separated by taxonomic ranks (red to pink rings) and colored by plankton functional groups in the scanner (**g**) and UVP (**h**) datasets. Blank portions correspond to organisms unassigned at the considered ranks, increasing in proportion for finer taxonomic ranks.

iron compounds found in marine ecosystems[38]. Labile compounds were mostly represented by aerosols, either from desert sources (best approximated by wet dust deposition satellite products) or from either volcanic and wildfire ashes or anthropogenic activities (all affecting the total aerosol optical thickness satellite product). A third proxy, representing the total iron concentration accounting for both mineral and organically-bound Fe ligands, from the biogeochemical model PISCES, was also tested given the similarity found between modeled concentrations and monthly average observations of in situ dissolved iron concentration measured as part of the GEOTRACES program (Supplementary Fig. 3). When iron proxies were excluded in our model construction, the total variance explained was reduced by 30-35% in the case of Rhizarians and Crustaceans, for which aerosol and total iron ranked second and first (together with integrated chlorophyll-a concentration) respectively, and by 20% for colonial $N_2$-fixers, whose biogeography appeared more linked to dust emissions alongside temperature (Table 1).

The temporal correlation between predicted abundances and the different iron proxies in individual grid cells (Supplementary Fig. 4) highlights the importance of mineral and other organically-bound iron proxies in mesoplankton model predictions (Fig. 3). The seasonal trends of NBSS predictions shows important similarities with dust and

https://doi.org/10.1038/s41467-026-75355-4

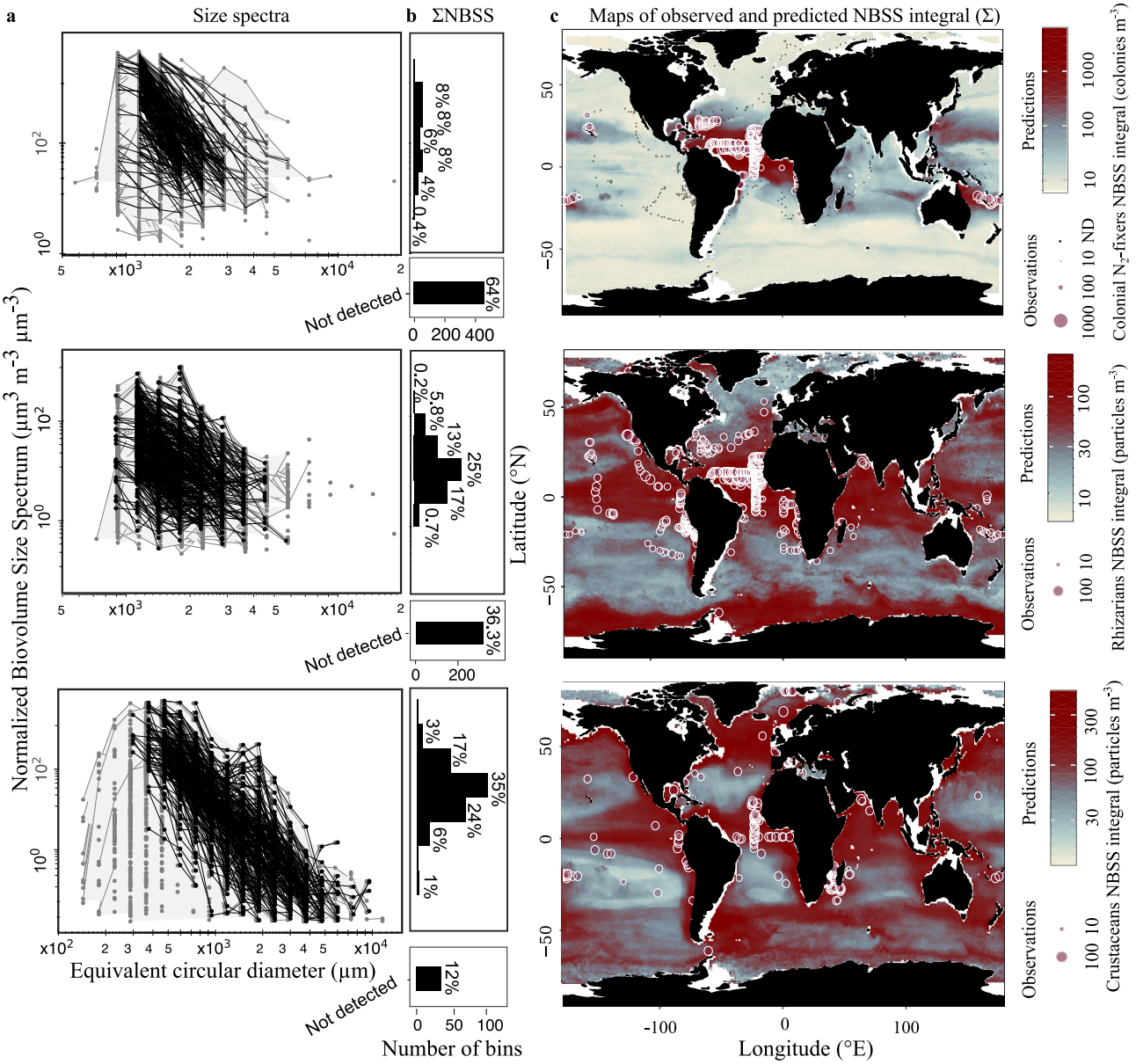


**Fig. 2 | Observed size spectra (left) and maps of observations and predictions (right) of colonial $N_2$-fixers (top panels), Rhizarians (middle panels), and Crustaceans (bottom panels) total abundance. a** Group-specific size spectra derived from Underwater Vision Profiler (for colonial $N_2$-fixers on top and Rhizarians in the middle) and scanner (for Crustaceans at the bottom) images. Gray dots mark size classes that were filtered out due to methodological bias (mesh of the nets, particles too rare to be counted accurately), and black dots indicate all final datapoints used to infer spectral parameters and predict Normalized Biovolume Size Spectrum (NBSS). Note that x-axis limits differ depending on the instrument resolution and detection limits. **b** Total abundance (ΣNBSS) of colonial $N_2$-fixers (top), Rhizarians (middle), and Crustaceans (bottom) in individual grid cells (1° × 1° longitude/latitude and year-month) distributed globally. Note that the y-axis is shared for (**a**, **b**). Number and percentage of empty records (not detected) are also indicated in separate sub-panels beneath each row. **c** Maps of observed (open circles) and predicted (colored tiles) average abundance, obtained by integrating NBSS estimates (Σ) using predicted parameters (slope, intercept, size range). ND: not detected.

aerosol proxies, ranked 1th and 5th in model's feature importance, suggesting a key role in shaping the size distribution of $N_2$-fixers in the Atlantic and Pacific subtropical gyres respectively (Fig. 3a, b, top panels). In the latter ecosystem, a main peak in abundance is observed in winter (Oct-Dec in the Northern hemisphere and Jun-Aug in the Southern hemisphere), consistent with a negative correlation between $N_2$-fixer abundances and light availability (Supplementary Table 1) and relatively high aerosol emissions (Fig. 3b). Correlations with aerosols were highest in the South Pacific Subtropical Gyre (SPSG), where anthropogenic dust is supplemented by ashes produced by volcanic activities or wildfires. In the Atlantic, where the main iron pool is provided by Saharan dust deposition, seasonal trends of $N_2$-fixer NBSS strongly followed the climatology of the dust product, marked by a peak of iron supply early in the year that progressively decreases to a minimum observed in June during the dry season. Similarly, $N_2$-fixer abundances were lowest in June and increased later in the year.

Likewise, both aerosols and wet dust deposition seemed to be driving the relatively high abundance of Rhizarians in most of the subtropical gyres (Fig. 3a, b, middle panels). The importance of aerosols was marked in several basins near the Equator, including in the Indian, Pacific, and Atlantic oceans. Observed correlation with specific classes of Rhizarians indicated that while aerosols were positively related to all classes, only Collodarians seemed to be favored by dust deposition ($r = 0.28$, Supplementary Table 1) with a peak in

https://doi.org/10.1038/s41467-026-75355-4

**Table 1 | Goodness of fit of mesoplankton size spectra predicted from a boosted regression tree model, tested with the full set of environmental factors or with a reduced model excluding all iron proxies**

| | Colonial $N_2$-fixers | | Rhizarians | | Crustaceans | |
|---|---|---|---|---|---|---|
| Model | Full | Reduced | Full | Reduced | Full | Reduced |
| $R^2$ | 0.93 | 0.76 | 0.88 | 0.57 | 0.79 | 0.56 |
| Rank: | Variables (feature importance metric): | | | | | |
| 1 | Wet dust deposition (0.21) | | Temperature (0.11) | | Chlorophyll concentration (0.11) | |
| 2 | Temperature (0.14) | | Aerosol (0.08) | | Total iron (0.11) | |
| 3 | Silicates (0.11) | | Phosphates (0.08) | | Temperature (0.09) | |
| 4 | Total iron (0.11) | | Wet dust deposition (0.07) | | Photosynthetic Available Radiance (0.08) | |
| 5 | Aerosol (0.06) | | Silicates (0.07) | | Sea Level Anomaly (0.07) | |
| 6 | Apparent Oxygen Utilization (0.05) | | Fraction of nanophytoplankton (0.06) | | Phosphates (0.06) | |
| 7 | Nitrates (0.04) | | Total iron (0.06) | | Particle Size Distribution slope (0.05) | |
| 8 | Mixed Layer Depth (0.03) | | Apparent Oxygen Utilization (0.0) | | Apparent Oxygen Utilization (0.05) | |
| 9 | Finite Size Lyapunov Exponent (0.03) | | Sea Level Anomaly (0.05) | | Aerosol (0.05) | |
| 10 | Net primary production (0.002) | | Nitrates (0.05) | | Nitrates (0.04) | |
| 11 | Chlorophyll concentration (0.02) | | Photosynthetic Available Radiance (0.05) | | Finite Size Lyapunov Exponent (0.04) | |
| 12 | Photosynthetic Available Radiance (0.02) | | Finite Size Lyapunov Exponent (0.05) | | Mixed Layer Depth (0.04) | |
| 13 | Phosphates (0.02) | | Mixed Layer Depth (0.04) | | Wet dust deposition (0.04) | |
| 14 | Sea Level Anomaly (0.02) | | Net primary production (0.04) | | Fraction of microphytoplankton (0.04) | |
| 15 | Fraction of nanophytoplankton (0.02) | | Fraction of microphytoplankton (0.03) | | Net primary production (0.03) | |
| 16 | Fraction of picophytoplankton (0.01) | | Chlorophyll concentration (0.03) | | Silicates (0.03) | |
| 17 | Fraction of microphytoplankton (0.01) | | Fraction of picophytoplankton (0.03) | | Fraction of picophytoplankton (0.03) | |
| 18 | Particle Size Distribution slope (0.01) | | Particle Size Distribution slope (0.03) | | Fraction of nanophytoplankton (0.02) | |

Ranking of environmental variables in the full model, expressing their importance in variance explained (in parentheses).

abundances marked after the input of Saharan dust during the wet season late in the year. Interestingly, the peak of modeled abundance of Rhizarians (Fig. 2c) in the Southern Ocean and upwelling ecosystems was likely linked to increased concentrations of total iron (Fig. 3a, b), as monthly average observations of in situ dissolved iron concentration measured as part of the GEOTRACES program also matched that of Rhizarian groups (i.e Phaeodaria and Foraminifera), with very high correlation coefficients ($r > 0.5$, Supplementary Table 1). This gives us further confidence in the linkages found between the total iron model product and mesoplankton spectral biogeography.

Compared to $N_2$-fixers and Rhizarians, Crustaceans were substantially linked to total iron concentration in all ecosystems (Fig. 3a, b, bottom panels). This result was also evident from the correlation with in situ observations from the GEOTRACES program, especially for copepods with respective coefficients of 0.26 with PISCES iron and 0.2 with GEOTRACES iron ($p$ value < 0.001, Supplementary Table 1). As a result, predictions of Crustacean total abundance closely followed the seasonal trends in total iron concentrations, especially in productive regions like temperate, polar, coastal, or upwelling ecosystems (Figs. 2c and 3c). In the North Pacific Temperate latitudes, Crustacean abundances increased in the spring, following the peak in microphytoplankton size fraction observed by satellite. Likewise, the pool of total iron presented a peak of concentration between Feb-Apr, following the increased Ekman pumping and deep mixing events occurring in the wintertime. In comparison, the wind-driven Ekman pumping located in the Eastern Equatorial Pacific is more sustained throughout the year[39], although Trade winds generally intensify between June-August, resulting in a small increase in total iron and overall weaker seasonal trends caused by upwelling (Fig. 3c). Yet, both the microphytoplankton fraction observed by satellite and our predictions of Crustacean abundances seemed to be linked to the overall availability of total iron in this ecosystem, with a concentration peak recorded in September. In polar ecosystems, our knowledge of seasonal trends is limited by the sea ice coverage, the lack of sunlight, and higher cloud coverage in the wintertime, as highlighted in important temporal and spatial gaps in both satellite and model products (Supplementary Fig. 2), resulting in only partial predictions of Crustaceans' size distribution at least in the Southern Ocean (Figs. 2 and 3). Despite such gaps, it appeared that total iron concentration and Crustacean abundances were higher during the austral summer than during the winter (Fig. 3c), which is unexpected given that phytoplankton blooms initiated in the summer are thought to considerably draw down iron concentrations in the upper ocean[40]. This phenomenon was even more apparent in the Arctic Ocean, where the demise of the spring bloom does not appear to cause a decline in both iron and Crustacean concentrations, which both remain relatively high through the end of the year.

## Adaptations and partitioning of spectral biogeography within broad mesoplankton groups in the upper ocean

Grouping image annotations by finer taxonomic resolution (classes in the case of Rhizarians and Crustaceans) or by morphotypes (in the case of colonial $N_2$-fixers) resulted in overall improved model performances compared to the full model presented above (Table 2), except for rare groups of Phaeodaria ($R^2 = 0.48$) and Foraminifera ($R^2 = 0.63$). The decrease in model information criteria (BIC and AIC estimates), indicative of improved fit, was more marginal for the colonial $N_2$-fixers due to the dominance of a specific class (i.e., Oscillatoriales) and morphotype (i.e., Tuff) in the UVP images (see data availability statement). In comparison, both Rhizarians and Crustaceans presented larger differences in model performance metrics when images were grouped in higher taxonomic ranks (classes or families) despite lower available observations, supporting strong evidence for their niche partitioning in the upper ocean. Using the same modeling approach applied to finer taxonomic groups, including copepods specific families that often

https://doi.org/10.1038/s41467-026-75355-4

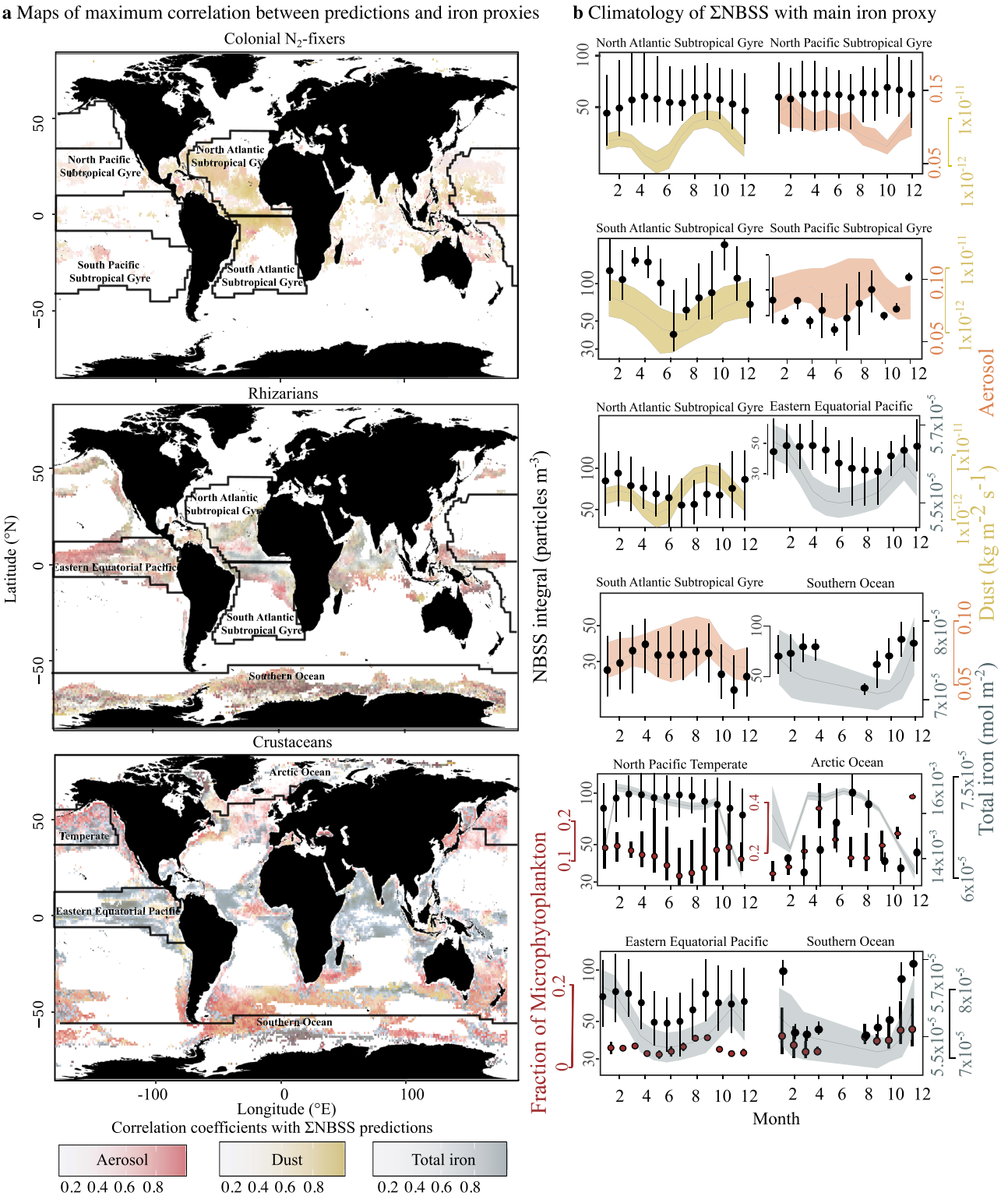


**Fig. 3 | Main iron proxies, aerosol (red), dust (yellow), or total iron (gray), linked to the spectral biogeography of colonial $N_2$-fixers (top panels), Rhizarians (middle panels), and Crustaceans (bottom panels). a** Maps of maximum correlation coefficients between predicted Normalized Biovolume Size Spectrum (NBSS) integral and iron proxies. The main iron proxy was attributed according to the variable that counted the most grid cells in specific ecosystems and ocean regions. Ecosystems whose climatology is presented in (**b**) are outlined in black. **b** Climatology of mesoplankton groups (black dots), total abundance (ΣNBSS), and the main iron proxy (ribbons) in ecosystems with significant correlations. Mean ± Standard deviations account for all simulations between 2008 and 2021, with $n = 14$. Seasonal trends of microphytoplankton (red dots) are superimposed on the climatology of Crustaceans NBSS integral to link their dynamics to that of phytoplankton prey.

**Table 2 | Statistical metrics to evaluate the goodness of fit of mesoplankton size spectra predictions in increasing taxonomic ranks**

| | Colonial $N_2$-fixers | | | Rhizarians | | Crustaceans | | |
|---|---|---|---|---|---|---|---|---|
| | Phylum | Family | FG | Phylum | Class | Phylum | Class | FG |
| Taxa | Cyanobacteria | Oscillatoriales | Puff Tuff | Radiozoa | Acantharia Collodaria Phaeodaria Foraminifera | Crustacea | Copepoda Malacostraca Ostracoda | Carnivore Omnivore |
| BIC | 152.2 | 151.3 | 149.8 | 149.5 | 135.3 | 152.6 | 136.6 | 130.0 |
| AIC | 150.3 | 150.2 | 148.5 | 148.1 | 135.7 | 159.5 | 136.1 | 130.6 |
| $R^2$ | 0.93 | 0.93 | 0.95 | 0.88 | 0.88 | 0.69 | 0.85 | 0.90 |
| | | | 0.95 | | 0.76 | | 0.96 | 0.92 |
| | | | | | 0.48 | | 0.92 | |
| | | | | | 0.63 | | | |

Functional groups (FG): Morphotypes for colonial $N_2$-fixers or trophic group for copepods according to the compilation of Benedetti et al.[41].
Optimal models are indicated by low AIC/BIC and high $R^2$.

correlate with a certain diet (e.g., omnivores or carnivores) as compiled in Benedetti et al.[41], we highlight the potential adaptations of these subgroups to certain environmental conditions. In the case of *Trichodesmium* morphotypes, differences in environmental linkages are indicative of plasticity, since multiple species can form either morphotype.

To identify the environmental factors involved in subgroup adaptations/plasticity and assess the degree of partitioning within subgroups, represented in Figs. 4–6a, we used the partial dependency responses of both spectral intercept and slope to all environmental factors tested. Partitioning was then calculated as the portion of the area under the curve that was not shared amongst all subgroups, which can be compared across environmental descriptors and also across broad mesoplankton phyla. Many iron proxies were involved in niche partitioning, indicating that the link between iron proxies and mesoplankton biogeography discussed in the section above was often caused by one, often dominant, taxon. For example, aerosol thickness seemed to promote both the intercept and slope of Puff ($r = 0.14$ and 0.22 respectively, Supplementary Table 1 and Fig. 4b) rather than Tuff colonies, which better responded to phosphate concentration ($r = -0.11$ and 0.07 respectively, Supplementary Table 1 and Fig. 4b). This distinction caused the former to be more abundant in regions where aerosols are released from hydrothermal vents near the Tonga islands and anthropogenic activities located in Asia in the Pacific Subtropical Gyres (Fig. 4c). Similarly, we found that both aerosol and dust emissions must contribute significantly to the hotspots of two mixotrophic Rhizarian classes, Collodarians and Acantharians, in the Atlantic and Pacific Gyres (Fig. 5c). Inversely, heterotrophic members like Phaeodaria and Foraminifera seemed more adapted to total iron concentrations, promoting larger colonies ($r = 0.22$ and 0.19 respectively, Supplementary Table 1 and Fig. 5b) that also benefited from higher chlorophyll-a concentration ($r = 0.24$ respectively, Supplementary Table 1 and Fig. 5b). As a result, these classes were dominant in productive systems located in polar regions, near the coasts, and in the upwelling system off the Californian coast (Fig. 5c). Total iron concentrations were also important in driving Crustaceans adaptations, as mostly Copepoda appeared correlated to increased trace metal availability, underlying the excessive dominance of Copepoda, especially omnivorous families, in polar and other productive ecosystems. Conversely, Ostracoda seemed more adapted to stratified ecosystems ($r$(Sea Surface Temperature, NBSS integral) = 0.34 and $r$(Mixed Layer Depth, NBSS integral) = −0.02) (Supplementary Table 1) located in the subtropics, while Malacostraca appeared to thrive under higher nitrate and silicate concentrations ($r = 0.15$) (Fig. 6).

Examples of second-order proxies involved in niche partitioning also included indicators of mesoscale circulation and availability of other nutrients, namely phosphates for colonial $N_2$-fixers, carnivorous copepods, and Foraminifera, silica for siliceous mixotrophic Rhizarians (e.g., Collodaria) and omnivorous copepods, or large prey (indicated by chlorophyll-a concentration, higher fraction of microphytoplankton, and lower absolute slope of the particle size distribution) for flux-feeding Phaeodaria, omnivorous copepods, and Malacostraca (Supplementary Table 1 and Figs. 4–6). By pairing class- or morphotype- specific spectral biogeography to mesoscale circulation proxies, we found that elevated concentrations of both Copepoda and Ostracoda were linked to cyclonic eddies (Fig. 6b), indicated by negative sea level anomalies ($r = -0.2$ and −0.16, respectively, Supplementary Table 1), as opposed to the class Malacostraca. While SLA did not impact the intercept of colonial $N_2$-fixers NBSS significantly, their slopes appeared relatively flatter in cyclonic eddies. Similarly, diverging fronts, indicated by a high absolute Lyapunov exponent, appeared to promote the accumulation of larger colonies of Tuff, likely through preferential attachments of individual filaments leading to the generation of long floating rafts at the surface of the Ocean ($r = -0.33$, $p$ value < 0.001).

## Discussion

### The spectral biogeography of mesoplankton groups in the upper ocean: Implications for present and future ecosystems functioning

In this study, we present a comprehensive analysis linking the size structure of colonial $N_2$-fixers (main autotrophic mesoplankton), Rhizarians (main mixotrophic mesoplankton), and Crustaceans (main heterotrophic mesoplankton), compiled from actual size observations to environmental gradients. We include diverse iron proxies to model and understand how spectral parameters vary in space and time, alongside traditional drivers like temperature, macronutrient/food availability, or upper ocean mesoscale features. Besides identifying potential drivers of trait distributions in the global ocean, our results provide insights into how mesoplankton affect marine ecosystems' biogeochemistry and services ($N_2$- and $CO_2$-fixation, carbon export, and micronutrient cycling) in response to environmental stressors. With the predictions of mesoplankton spectral biogeography and associated compilations of pelagic size spectra, expressed as a function of cell abundances or carbon biomass, our hope is to inform the development of biogeochemical and other size-structured models used to foresee the changes in ecosystem functioning and services under future climate change. Indeed, the complexity of plankton functional types represented in the Coupled Model Intercomparison Project 6 models has significantly increased with the support of dataset compilations (e.g., MAREDAT, COPEPOD), representing bulk biomass estimates so far. Since plankton functional type and size structure, rather than bulk biomass and productivity estimates, is considered the best predictor of ecosystem services like fish production or carbon export, our dataset should represent a good

https://doi.org/10.1038/s41467-026-75355-4

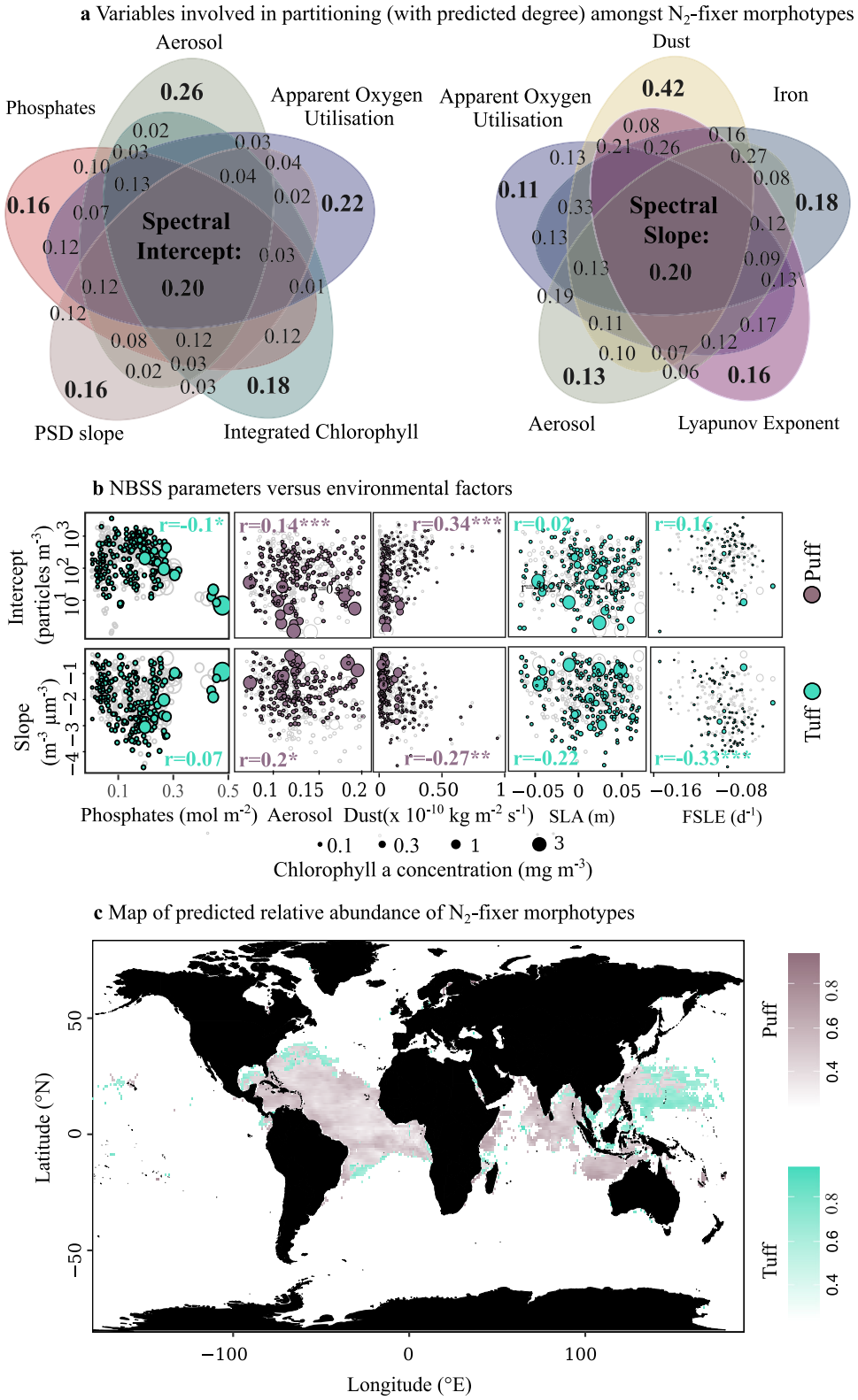


**Fig. 4 | Environmental plasticity of colonial $N_2$-fixers morphotypes. a** Venn diagram representing the top-5 stressors involved in morphotype partitioning (numbers represent the degree of partitioning) based on partial dependence plots for spectral intercept (left diagram) and slope (right diagram). **b** Correlations between environmental factors and Tuff (green dots) or Puff (brown dots) NBSS parameters (slope and intercept). Datapoints vary in size according to the surface chlorophyll-a concentration in that same bin. **c** Predicted maps of colonial $N_2$-fixers morphotypes relative abundance (same color code). SLA sea level anomaly, FSLE finite size Lyapunov exponent, PSD particle size distribution. Significance levels for Spearman correlation coefficients: *: 0.05, **: 0.01, ***: 0.001. *P* values: *r*(intercept, phosphates): 0.02, *r*(intercept, aerosol):0, *r*(slope, aerosol): 0.006, *r*(intercept, dust): 0, *r*(slope, FSLE): 0.0002.

https://doi.org/10.1038/s41467-026-75355-4

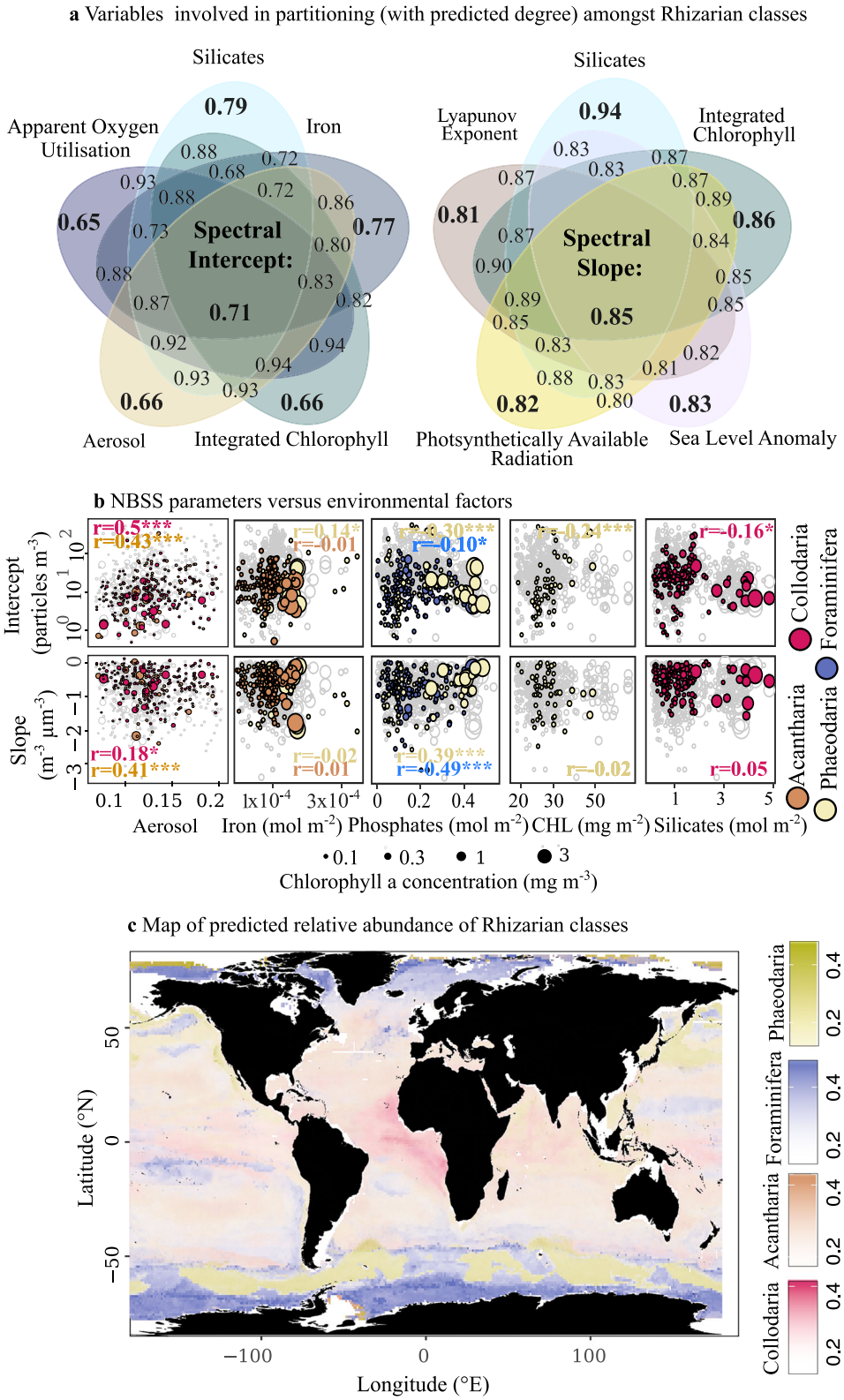


**Fig. 5 | Environmental adaptations within Rhizarian classes. a** Venn diagram representing the top-5 stressors involved in classes partitioning (numbers represent the degree of partitioning) based on partial dependence plots for spectral intercept (left diagram) and slope (right diagram). **b** Correlations between environmental factors and Acantharia (orange), Collodaria (pink), Foraminifera (blue), or Phaeodaria(yellow) NBSS parameters (slope and intercept). Datapoints vary in size according to the surface chlorophyll-a concentration in that same bin. **c** Predicted maps of Rhizarian classes relative abundance (same color code). CHL: integrated chlorophyll-a concentration. Significance levels for Spearman correlation coefficients: *: 0.05, **: 0.01, ***: 0.001. *P* values: *r*(Acantharia intercept, aerosol): 0, *r*(Collodaria intercept, aerosol): 0, *r*(Acantharia slope, aerosol): 0.0004, *r*(Collodaria slope, aerosol): 0.01, *r*(Phaeodaria intercept, iron): 0.03, *r*(Acantharia intercept, phosphates): 0, *r*(Foraminifera intercept, phosphates): 0.04, *r*(Phaeodaria slope, phosphates): 0, *r*(Foraminifera slope, phosphates):0, *r*(Phaeodaria intercept, CHL): 0, *r*(Collodaria intercept, silicates): 0.04.

https://doi.org/10.1038/s41467-026-75355-4

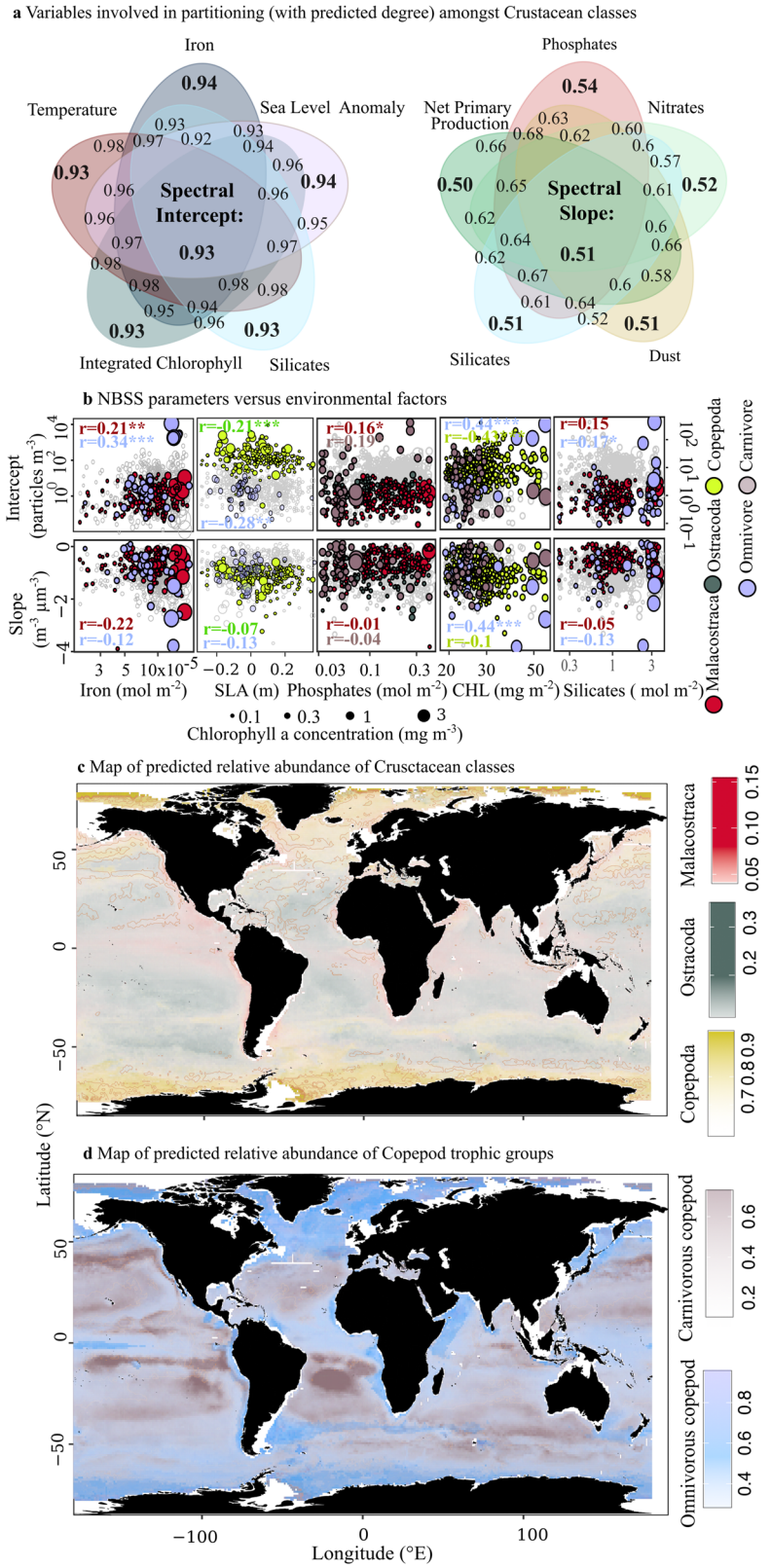


**Fig. 6 | Environmental adaptations within Crustacean classes and trophic groups. a** Venn diagram representing the top-5 stressors involved in classes partitioning (numbers represent the degree of partitioning) based on partial dependence plots for spectral intercept (left diagram) and slope (right diagram). **b** Correlations between environmental factors and Copepoda (yellow), Ostracoda (green), Malacostraca (red), and copepod functional groups (omnivore in blue, carnivore in gray) NBSS parameters (slope and intercept). Datapoints vary in size according to the surface chlorophyll-a concentration in that same bin. **c** Predicted maps of Crustacean classes relative abundance (same color code). SLA: sea level anomaly, CHL: integrated chlorophyll-a concentration. Significance levels for Spearman correlation coefficients: *: 0.05, **: 0.01, ***: 0.001. *P* values *r*(Malacostraca intercept, iron) 0.002, *r*(Omnivore intercept, iron) 0.0005, *r*(Copepoda intercept, SLA) 0.00001, *r*(Malacostraca intercept, phosphates) 0.03, *r*(Omnivore intercept, CHL) 0.0005, *r*(Copepoda intercept, CHL):0, *r*(Omnivore slope, CHL) 0, *r*(Omnivore intercept, silicates) 0.015.

opportunity to examine the effects of climate change multi-faceted stressors on essential marine ecosystem services.

In essence, our findings revealed that temperature remains a primary factor influencing large-scale shifts in mesoplankton size. Although their overall abundance showed contrasting correlations with average temperature, all groups showed a negative correlation between spectral slopes and average temperature ($r$(Colonial $N_2$-fixers) = −0.22, $r$(Rhizarians) = −0.28, $r$(Crustaceans) = −0.43, $p$ values < 0.001), indicating that larger organisms were mostly found in relatively colder environments: a general trend underpinning the Temperature-Size Rule[23]. The first hypothesis explaining the emergence of larger metazoans in cold environments was linked to increased oxygen availability[23], since spatial gradients in surface temperature are opposed to that of dissolved oxygen in marine ecosystems (Supplementary Fig. 2). Oxygen exerts a strong metabolic constraint on Crustaceans, with concentrations between 15 and 50 μM of dissolved oxygen typically defined as critical to maintain aerobic reactions and survival[42,43]. All Crustacean groups showed a positive correlation between spectral slopes and dissolved oxygen concentration ($r$ = 0.26 for Copepoda, 0.22 for Ostracoda, or 0.08 for Malacrostraca), indicating a flattening of their spectra under high oxygen concentrations. Since endosymbiotic Rhizarians and colonial $N_2$-fixers do not require high oxygen concentration to fuel their metabolism (they rather support the production or directly produce oxygen by photosynthesis), it is unlikely that oxygen levels are responsible for the Temperature-Size Rule observed for these groups. Instead, we hypothesize that the apparent Temperature-Size Rule in colonial $N_2$-fixers and Rhizarians invokes differences in anabolic (i.e growth) versus catabolic (i.e respiration) rates with respect to changes in temperature. These are typically quantified over a 10 °C change, and referred to as temperature coefficients ($Q_{10}$). Catabolic rates should increase more rapidly with temperature compared to anabolic reactions in comparatively smaller organisms, as organisms that present higher $Q_{10}$ coefficients for respiration than for growth[44]. High respiration rates at high temperatures were shown to support the anoxic conditions that favor $N_2$-fixation within colonies of *Trichodesmium*[45–47]. Plus, $Q_{10}$ measured from enclosed experiments with Foraminifera[48] or Collodaria[49] suggests that similar regulatory effects on metabolic reactions may come into play for symbiotic Rhizarians to explain the negative correlation between temperature and their spectral slopes. Our results therefore directly support published meta-analysis[50] in suggesting that increased warming and deoxygenation of future marine ecosystems should decrease the size of most mesoplankton groups in the upper ocean, likely disrupting both fisheries[51,52] and carbon export through reduced gravitational sinking[53–55] and fecal pellet production[12].

Our study also highlights several aspects of ecosystem functioning that may limit the negative impacts of global warming and deoxygenation in the upper ocean. Compared to previous findings, we captured more variance of mesoplankton trait biogeographies in space and time, with $R^2$ of 0.93, 0.88, and 0.79 for $N_2$-fixers, Rhizarians, and Crustaceans, respectively, largely due to the inclusion of various iron proxies underlining the strong linkage between keystone mesoplankton and trace element cycling. Each phylum responded best to a different proxy of iron supply in the epipelagic layer, with a noticeable stimulation of dust and other aeolian iron-rich compounds on the sizes and occurrences of large mixotrophic Rhizarians (e.g., Collodaria, Acantharia) and colonial $N_2$-fixers, and a strong link between Crustaceans' biogeography and total iron concentrations. While the peak of $N_2$-fixing *Trichodesmium* abundance in the Subtropical Atlantic has already been largely attributed to Saharan dust deposition in this ecosystem[56–58], we also found a significant relationship between wet dust deposition and occurrences of Rhizarians. To our knowledge, this relationship has not been demonstrated before and could point to an interesting adaptation of mixotrophic Collodaria and Acantharia, which would require follow-up studies. In the Pacific Ocean, the same groups responded mainly to elevated aerosol fluxes. Phytoplankton blooms, followed by satellite chlorophyll-a concentration, have been regularly linked to direct ash deposition from Southern Pacific tropical islands (Papua New Guinea, Vanuatu and more recently Tonga) volcanic eruptions[59], Australian wildfires[60], and recently to shallow hydrothermal emissions located across the Tonga-Kermadec volcanic arc[61]. The latter have been implicated in the iron fertilization of surface waters, leading to elevated concentrations of $N_2$-fixers[62], more specifically *Trichodesmium*, and a shift in the mesoplankton community[63]. Zooscan analyses highlighted the presence of gelatinous zooplankton in the vicinity of the volcanic arc, in an ecosystem otherwise dominated by copepods. Since nets severely damage the fragile Rhizarians, it was not possible to quantify the impact of iron supply by volcanic emissions, and more generally by aerosols, on this taxonomic group. Our predictions of Rhizarian NBSS appeared linked to aerosol proxy in the SPSG, suggesting that volcanic ashes could also promote the growth of symbiotic Rhizarians like Acantharia and Collodaria. According to the latest CMIP6 simulations, natural dust deposition should increase by 7–20% by the end of the century as a result of enhanced desertification and precipitation, as well as changes in wind regimes and land use[64–66], thus potentially promoting carbon and nitrogen fixation in the low and mid-latitude ecosystems by mixotrophic Rhizarians and colonial $N_2$-fixers. Further, even though aerosol emissions from anthropogenic activities should decline by 50–80% to meet higher air quality standards and the 1.5 °C global warming target above pre-industrial levels dictated by the Paris agreement by the mid twenty-first century[65], aerosol distribution might also be impacted by alternative natural sources whose emissions could increase up to 125% under global warming according to the CMIP6 models[66].

Even though we expected these different iron proxies to be important stressors of mesoplankton biogeography, especially for the autotrophic colonial $N_2$-fixers, the ranking of total iron concentration in relation to the spectral biogeography of Crustaceans was the most surprising given that we also included satellite proxies for phytoplankton producitivity (i.e integrated chlorophyll-a concentration and net primary production) or size distribution (slope and fraction of pico-, nano-, and microphytoplankton) in the full model. The coupling between climatologies of satellite microphytoplankton, model total iron concentrations, and predicted Crustacean occurrences in the Equatorial Pacific, California Current upwelling systems, Southern Ocean, subarctic Pacific, and subpolar North Atlantic supports the long-standing recognition that dissolved iron exerts a strong control on phytoplankton dynamics[67] and associated grazers in the High Nutrient Low Chlorophyll ecosystems. Further, the increased concentration of total iron and Crustaceans during and after phytoplankton blooms in polar latitudes highlights the possible role of secondary producers in alleviating nutrient limitation, as noted in Tagliabue et al.[40]: higher dissolved iron concentrations associated with high chlorophyll-a could be reconciled by assuming high rates of Fe recycling associated with greater biomass. Iron fertilization experiments have confirmed the importance of copepods in driving iron recycling and further sustaining phytoplankton blooms in both the Southern[68] and the Arctic Ocean[69], even though exogenous inputs of iron by river discharges could also be partly responsible for the peak concentration observed after the spring bloom in this ecosystem[70]. Moreover, a recent comparison between a compilation of total dissolved iron and gridded products[71] similar to our analysis has shown that iron was strongly correlated to Apparent Oxygen Utilization (AOU), which appears positively correlated to Copepod biogeography in our analysis (Supplementary Table 1). These empirical evidence, together with our global analysis linking iron pool to mesozooplankton spectral biogeography, suggest that Crustaceans could maintain elevated iron concentrations by preying on large phytoplankton and remineralizing organic iron into bioavailable forms,

further alleviating nutrient limitation of their prey, thus exerting a positive feedback loop that could offset the decline of primary production caused by enhanced stratification and reduced nutrient delivery.

## Methods

### Global compilation of group-specific size spectrum

To understand and predict the global size distribution of colonial $N_2$-fixers, Rhizarians, and Crustaceans in the epipelagic layer, we compiled direct size estimates measured by a range of UVPs of successive generations[72,73] and benchtop scanners like the ZooScan[74] for nets deployed in all major basins within 0 and 200 m. This compilation stems from a collaborative, international effort, termed the Pelagic Size Structure database (https://pssdb.net), that aims at providing standardized and homogenized size and count information collected by a variety of commercially available plankton imaging instruments. We used the Python workflow (publicly available at https://github.com/jessluo/PSSdb) developed for the first PSSdb release[75], with little modifications to produce our globally consistent estimates of group-specific Normalized Biovolume Size Spectra (hereafter referred to as NBSS).

Briefly, the general pipeline consists in five automated steps that follow image acquisition and near-real time segmentation (i.e., the process of separating individual particles from background pixels to extract their morphologic features)[1]: export of raw size, count and annotation information with the associated metadata from the collaborative platform for image annotation EcoTaxa (https://ecotaxa.obs-vlfr.fr/)[2], standardization of the export tables following a unique format with standard labels and units[3], quality control of individual datasets that account for particle count uncertainty, sufficient manual validation of the taxonomic classifications (UVP profiles of scanned nets should have ≥95% validated annotations to pass our quality control), differences in size calibration factors, missing information or incorrect GPS location of each sample[4], aggregation of samples collected in spatial and temporal proximity to provide accurate measures of particle size distribution at the current resolution of biogeochemical models and other global data compilations (i.e., 1° × 1° latitude/longitude and year/month), and[5] the computation of NBSS and derived parameters (slope, intercept, $R^2$), using pre-defined size classes matching the recent compilation of UVP5 particle size distribution by Kiko et al.[76].

The main addition to the Dugenne et al.[75] workflow consists of standardizing all taxonomic annotations assigned to individual particles by automated classifiers and later validated by taxonomic experts using the World Register of Marine Species (https://www.marinespecies.org/) as suggested in Neeley et al.[77]. We wrote a custom script based on existing web scraping functions to automatically search for the taxonomic annotations in WORMS, allowing various formats (e.g., hierarchical or nominal category) and ranks according to the preset classes of automated classifiers, the expertise of human annotators or the research question. The taxonomic look-up table automatically generated by this script is available at https://github.com/jessluo/PSSdb/blob/main/ancillary/plankton_annotated_taxonomy.xlsx. Following this additional standardization, individual annotations were grouped in increasing taxonomic ranks (e.g., phylum, class or subclass, family to assign copepods' trophic strategy based on published compilation) and according to their morphotypes when possible (e.g., solitary or colonial for Rhizarians, Puff or Tuff for *Trichodesmium)* to estimate group-specific NBSS based on biovolume. Biovolume estimates were computed using equivalent circular diameter (ECD) derived from particles area following Eq. (1):

$$\text{Biovolume}(\mu\text{m}^3) = \tfrac{1}{6} \times \pi \times \text{ECD}(\mu\text{m})^3 = \tfrac{1}{6} \times \pi \times \left(2\sqrt{\frac{\text{area}\,(\mu\text{m}^2)}{\pi}}\right)3 \quad (1)$$

The sum of all biovolume estimates within the discrete size classes defined in Eq. (2) is then normalized to the volume analyzed, corresponding to the total volume cumulated over depth (0–200 m) and within each spatio-temporal bin, and to the width of each size class to produce NBSS according to Eq. (3).

$$\text{ECD}_i(\mu\text{m}) = 2^{i \times 1/3} \text{ with i} = 0, 1, \ldots, 78 \text{ for size classes ranging between 1} - 53,000,000\mu\text{m} \quad (2)$$

$$\text{NBSS}_i\ (\mu\text{m}^3\,\text{m}^{-3}\,\mu\text{m}^{-3}) = \sum_i \text{Biovolume/volume analyzed} \,/\text{biovolume class width} \quad (3)$$

We then selected the maximum and the last normalized biovolume estimate before observing one empty size class, respectively, as the lower and upper limits of each size spectrum. This step is necessary to select the effective size range of the individual mesoplankton group and to ensure that estimates are not biased by the camera resolution or the sampling gear (e.g., net mesh), or by the limited volume sampled, respectively. After selection, unbiased NBSS estimates and associated midpoint of individual biovolume size classes are $\log_{10}$-transformed to estimate spectral slopes, intercepts, and size ranges for each 1° × 1° latitude/longitude and year-month by linear regression (Supplementary Fig. 1). Intercept estimates were scaled to the minimum observed size of individual mesoplankton groups since the abundance of 1 $\mu m^3$ particles, the initial intercept for a spectrum starting at $\log(1\,\mu m^3) = 0$, is not representative of the actual abundance of mesoplankton groups. Some of the individual spatio-temporal bins did not contain enough observations to construct a reliable NBSS and fit a log-linear regression, as group-specific PSSdb products necessarily included fewer images than the first release. In addition, we selected only datasets that spanned at least 80% of the epipelagic layer (e.g., 160 m) to follow the methodology established by Drago et al.[78]. As a result, the spatio-temporal coverage in our study is slightly diminished compared to the bulk datasets, constructed with all particles imaged except for methodological artifacts. Overall, group-specific NBSS were computed using 3068 UVP profiles and 2411 scans sampled between 2008 and 2021 and 2004 and 2022, respectively. These new products can be downloaded at https://doi.org/10.5281/zenodo.10810190.

### Linkages between mesoplankton size structure and environmental covariates

In the absence of broadly concurrent and quality-controlled in situ hydrographic measurements, we linked mesoplankton NBSS to environmental gradients using global sets of objective analysis, satellite proxies, and biogeochemical models (all accessed and downloaded in Sept. 2023). We used the latest World Ocean Atlas[79] objective analysis (WOA, available at https://www.ncei.noaa.gov/access/world-ocean-atlas-2018) to assign each grid cell (defined by 1° × 1° latitude/longitude and month) its associated mean mixed layer depth (m), along with the 0–200 m average temperature (°C), and integrated concentration in phosphate (mol $m^{-2}$), silicate (mol $m^{-2}$), or nitrate (mol $m^{-2}$). In addition, we used WOA integrated AOU (mol $m^{-2}$) to represent patterns in dissolved oxygen concentration resulting from water mass ventilation and age or remineralization rather than the temperature-dependent $O_2$ solubility.

Given that iron is also considered an essential micronutrient for phytoplankton growth[67] but in situ measurements are still too scarce to construct a reliable distribution of dissolved iron concentrations in the global ocean with enough temporal coverage[80], we relied on diverse proxies, satellite measurements distributed by NASA; biogeochemical models provided by Copernicus, of both mineral and total iron compounds, respectively. In the surface ocean, most labile compounds present are thought to originate from atmospheric aerosols,

delivering mineral dust, ashes formed by volcanic activities and wildfires, or anthropogenic compounds, all relatively rich in iron[38]. These can be approximated from space, as total aerosol optical thickness (unitless variable termed Aerosol optical thickness at 869 nm) and wet dust deposition (variable termed dust wet deposition bin 001 or duwt001, in $kg\,m^{-2}\,s^{-1}$), with a 9 km, monthly resolution using specific satellite algorithms whose products are distributed for every year and month by NASA at https://oceandata.sci.gsfc.nasa.gov/directdataaccess/Level-3%20Mapped/Aqua-MODIS and https://goldsmr4.gesdisc.eosdis.nasa.gov/opendap/MERRA2_MONTHLY/M2TMNXADG.5.12.4/ respectively. Alternatively, organic iron-complexing ligands can also represent important sources of iron, especially for organisms synthesizing siderophore transporters, which are poorly characterized by current analytical methods due to the diversity of compounds and reactivity within this pool[81]. To account for all compounds in the complex pool of dissolved iron, we used 0–200 m integrated predictions of total dissolved iron concentration ($mol\,m^{-2}$) from the biogeochemical model PISCES[82], distributed for any given year, month within the period 1993–2022 by Copernicus (product cmems_mod_glo_bgc_my_0.25_P1M-m available at https://data.marine.copernicus.eu/product/GLOBAL_MULTIYEAR_BGC_001_029/) with a resolution of 1/4° latitude/longitude. This model has shown a strong agreement with benchmark sections from the GEOTRACES program compared to other model predictions and also includes all known source and sink processes (riverine, sediment, hydrothermal, or dust inputs, remineralization, scavenging) affecting iron pools in marine ecosystems[80].

We downloaded monthly integrated photosynthetically available radiation (PAR, in $E\,m^{-2}\,d^{-1}$) and surface chlorophyll-a concentration for all sampled years (2004–2022) from the same URL as the aerosol NASA satellite products. The latter products were converted to integrated chlorophyll-a concentration (CHL, in $mg\,m^{-2}$) using the general formula published in Tanner et al.[83], adapted to fit concurring chlorophyll concentration profiles measured by biogeochemical-Argo profiling floats. In addition, we used integrated net primary production gridded products, parameterized with satellite inherent optical properties and phytoplankton growth rates, downloaded from http://www.science.oregonstate.edu/ocean.productivity/ following Silsbe et al.[84]. Besides integrated chlorophyll-a concentration and net primary production, we also included recent surface estimates of the particle size distribution slope (PSD slope, in particles $L^{-1}\,\mu m^{-2}$) and fractions of pico- (0.2–2 μm), nano- (2–20 μm), and micro- (20–50 μm) phytoplankton retrieved from backscatter coefficients measured by remote sensing at a resolution 4 km for every month year[85] to characterize the phytoplankton community representing the main food source for mesozooplankton groups. Lastly, proxies for mesoscale structure, like sea level anomaly (SLA, in m), that indicate cyclonic and anticyclonic eddies under negative and positive anomaly, and finite size Lyapunov exponent (FSLE, in $d^{-1}$), that measures the frontal divergence of mesoscale eddies or other currents in close proximity, were accessed on AVISO at https://www.aviso.altimetry.fr/en/data/products with a resolution of 1/25° latitude/longitude. Since mesoscale features are operationally defined as coherent vortex generally trackable for a month or longer with a radius scale of ~100 km[86], we consider that the final 1° × 1° (~111 km) and year-month resolution of our datasets were also representative of mesoscale circulation, even at the higher end member of its operational resolution.

All variables were automatically downloaded and averaged to match the resolution of our mesoplankton NBSS estimates (if the resolution was greater than 1° × 1° latitude/longitude and year, month) using custom scripts available at https://github.com/mdugenne/PSSdb_Learning. Resulting spatial patterns are presented in Supplementary Fig. 3. The environmental datasets were then merged to our group-specific products according to the bin location (1° × 1° latitude/longitude) and the sampling time (year, month for yearly resolved variables or month for WOA climatologies). Locations with one or more missing environmental variable(s) (e.g., satellite products at high latitude during winter) were filtered out to compute the Spearman correlation coefficients between environmental factors and spectral parameters (slope, intercept, size range) and train the machine learning model used to predict the size distribution of mesoplankton groups globally. The scripts allow predictions with both depth-integrated and surface covariates in case groups were more abundant in the surface layer. In this study, model performances increased significantly with depth-integrated covariates, especially for Rhizarians (from 0.61 to 0.88) and Crustaceans (from 0.69 to 0.79), while staying similar for colonial $N_2$-fixers, as they are typically found in greater abundances in the surface (see code availability statement).

### Global predictions of mesoplankton size structure using machine learning models

We used our compilations of group-specific NBSS and associated environmental factors in combination with machine learning habitat models to estimate the global size distribution of the three major mesoplankton groups (Colonial $N_2$-fixers, Rhizarians, Crustaceans) in the epipelagic layer. Like Barton et al.[21], we recognize that mesoplankton size biogeography is ultimately determined by the interplay between both bottom-up and top-down (e.g., size-selective predation by fish or other nekton) controls, though the latter are out of this paper's scope as this would require an extensive characterization of larger predators (through space and time) that are poorly detected with the imaging systems we used. Hence, our results underscore the importance of specific covariates that may vary with the inclusion of other global gridded datasets.

Our modeling effort builds on the recent publication of Drago et al.[78], who characterized and predicted the total biomass estimates of several mesozooplankton groups (e.g., Copepods, Rhizarians, not including colonial $N_2$-fixers) using UVP profiles globally distributed. Since elevated biomass may result from increased abundance and/or size, we expanded their work to help disentangle the effect of environmental factors on mesoplankton abundance (with the maximum abundance representing the spectral intercept) and size (whose continuum is determined by spectral slopes and effective range). Habitat models cover diverse statistical models, including the relatively recent boosted regression trees (also referred to as xgboost, ref. 87), that link environmental factors to species or group distribution with the objective to predict their occurrence in unsampled locations. Like other machine learning models, xgboost learns simple or complex rules (here a hierarchy of yes/no decisions delimited by the maximum tree depth) linking the response variable (NBSS parameters) to explanatory variables (environmental factors described in the "Methods" section "Linkages between mesoplankton size structure and environmental covariates") using a subset of the dataset (here 80% random split), named the training set. The learning process is an iterative process based on the progressive evaluation of a loss function, defined as the root mean square error between observations and predictions.

Their performance is then assessed using the remaining subset (here, 20% random split), termed the test set. The algorithm performance evaluation is based on different metrics like the coefficient of determination ($R^2$), determined by the sum of squared errors between test predictions and the test set, or the log-likelihood of the model, which represents the goodness of fit between model predictions and observations according to the data distribution. We used two parameters linked to the model log-likelihood (noted $l$), the Akaike (AIC) and Bayesian (BIC) Information Criterion defined in Eq. (4), to compare model predictions amongst increasing taxonomic ranks. While we expect that grouping observations based on high taxonomic rank, like class or families, should be more appropriate to capture the variability in mesoplankton NBSS on a global scale as a result of diverging

environmental adaptations[24], we also considered that the decrease of available observations for these ranks or the differences in model complexity could also result in overall lower performances of the model. Since AIC and BIC take into account model likelihood, complexity, and the number of available observations, we used these estimates as a means to provide objective comparisons between model performances. The likelihood of taxon-specific models was averaged, with a weight corresponding to the proportion of observations, across all subgroups of colonial $N_2$-fixers, Rhizarians, and Crustaceans when increased taxonomic ranks were compared to the overall model performed at the phylum level, following a similar approach as mixture models[88].

$$\mathrm{AIC} = 2k - 2l \text{ and } \mathrm{BIC} = k \times \ln(n) - 2l, \quad (4)$$

with $k$ the number of model parameters, $n$ the number of observations, and $l$ the model log-likelihood directly returned by the xgboost package.

Unlike more traditional decision tree models that predict a set of discrete values termed the leaves, xgboost models may apply to continuous variables by producing numerous leaves associated with a specific score, which are ultimately summed up across all trees to create a smooth gradient in the predicted response variable (i.e the boosting process). Instead of discontinuous response, the resulting predictions will thus present a smoother data distribution similar to that of spectral parameters (Supplementary Fig. 1). Since these models are based on direct representation of the linkages between explanatory and response variables, estimates of feature importance, measured as the average gain in model performance (log-likelihood) across all splits after the variable was used, are relatively straightforward. Such models have additional advantages as they can deal with many dependent variables (for example, dust and aerosol proxies for iron deposition, or temperature and PAR) and predict multivariate outputs. In our study, we simultaneously predicted spectral slopes, intercepts, and size range while accounting for their correlation (Supplementary Fig. 1). The reconstructed NBSS, obtained by assuming a log-linear decline with the modeled parameters, can then be integrated to predict the total abundances of mesoplankton groups at any given space and time. 50 model predictions were performed on bootstrapped observations in order to estimate model uncertainties represented by the predicted coefficients of variation (Supplementary Fig. 2). Prior to model training, both the spectral intercept and size range were $\log_{10}$-transformed to ensure that predictions will be positive after reverse transformation. To minimize the effect of irrelevant explanatory variables and avoid model overfitting, several parameters were tuned, including score shrinkage (eta parameter tested between 0.1 and 0.5) to homogenize the gradient boosting process in case of overfitting, the maximum number of splits in the decision trees (max_depth parameter tested between 3 and 10) that can lead to oversimplification/complexification of the model, or the number of trees (n_estimators parameter tested between 20 and 100). The best combination of model parameters was determined objectively using the grid search function implemented in the xgboost package.

Not all mesoplankton groups were abundant enough or significantly correlated with the environmental factors tested to analyze and predict their size structure in the epipelagic layer using a machine learning model[78]. Overall, we could accurately predict (i.e., with high $R^2$) the spectral biogeography of one family of colonial $N_2$-fixers (Oscillatoriales), four classes of Rhizarians (Acantharia, Collodaria, Phaeodaria, Foraminifera), and three classes of Crustaceans (Copepoda, Malacostraca, Ostracoda). The family of colonial $N_2$-fixers was represented exclusively by *Trichodesmium* in this study, although we note the presence of a few Nostocales in the Baltic Sea that were too rare for reliable predictions of their size spectrum (see data availability statement). Some groups were further distinguished based on their morphology (e.g., *Trichodesmium* puff or tuff), or into functional groups (e.g., carnivorous or omnivorous copepods) based on published correspondence between copepods' families and trophic groups[41]. Classes of Rhizaria were almost exclusively found as solitary (Collodaria) or colonial (Phaeodaria, Foraminifera) forms in the epipelagic, so we could not explore possible niche partitioning amongst colonial and solitary Rhizarians. Predictions were generated with the optimal set of parameters in every 1° × 1° grid cell for the full temporal coverage of the UVP and scanners datasets. Temporal correlations with the multiple iron proxies (total iron, dust or aerosol) were estimated in each spatial bin to determine which proxy had the strongest link with NBSS integral predictions, that result from predicted slopes, intercepts and size ranges (Supplementary Fig. 4). The main iron proxy was then defined based on the maximum correlation across the 3 possible correlation coefficients in broad ecosystem categories (e.g., Polar, Temperate-Subpolar, Subtropical Gyres, Equatorial-Upwellings) corresponding to adjacent Longhurst provinces (https://www.marineregions.org/sources.php#longhurst), and in diverse ocean basins (https://www.marineregions.org/sources.php#goas). For a full description of the xgboost Python package used in this study, see the documentation provided at https://xgboost.readthedocs.io/en/stable/python. The code to train, check the model performance and feature importance, and predict mesoplankton size distribution based on xgboost functions is available at https://github.com/mdugenne/PSSdb_Learning.

### Reporting summary

Further information on research design is available in the Nature Portfolio Reporting Summary linked to this article.

## Data availability

The datasets used in this study have been deposited in the Zenodo repository under accession code: https://doi.org/10.5281/zenodo.10810190. Raw data sources can be accessed on EcoTaxa (https://ecotaxa.obs-vlfr.fr/) under project ID: 3, 4, 22, 28, 36, 37, 38, 110, 507, 545, 548, 556, 558, 559, 560, 563, 578, 579, 584, 585, 586, 587, 588, 589, 590, 593, 594, 595, 602, 603, 610, 620, 621, 622, 881, 1343, 1591, 2464, 2465, 4028, 4041, 5690, 5693, 7546, 14, 167, 271, 174, 338, 358, 371, 372, 377, 378, 395, 397, 398, 412, 418, 474, 477, 486, 493, 516, 517, 528, 530, 532, 580, 581, 652, 663, 709, 710, 711, 714, 751, 752, 788, 896, 966, 967, 968, 1309, 1603, 2307, 2480, 2535, 2771, 2832, 2979, 2980, 2989, 3391, 3607, 4024, 4025, 4429, 4598, 4904, 5260, 5262, 5304, 6048, 6111, 6212, 8788, 884. Model outputs can be downloaded at https://github.com/mdugenne/PSSdb_Learning (https://doi.org/10.5281/zenodo.20559579).

## Code availability

Code to generate the datasets from raw data sources can be found at: https://github.com/jessluo/PSSdb. Code to generate model outputs is available at: https://github.com/mdugenne/PSSdb_Learning (https://doi.org/10.5281/zenodo.20559579).

## References

1. Sheldon, R. W., Prakash, A. & Sutcliffe, W. H. Jr. The size distribution of particles in the Ocean. *Limnol. Oceanogr.* **17**, 327–340 (1972).
2. Platt, T. & Denman, K. Organisation in the pelagic ecosystem. *Helgol. Wiss. Meeresunters.* **30**, 575–581 (1977).
3. Petchey, O. L. & Belgrano, A. Body-size distributions and size-spectra: universal indicators of ecological status? *Biol. Lett.* **6**, 434–437 (2010).
4. Trebilco, R., Baum, J. K., Salomon, A. K. & Dulvy, N. K. Ecosystem ecology: size-based constraints on the pyramids of life. *Trends Ecol. Evol.* **28**, 423–431 (2013).
5. Henson, S., Le Moigne, F. & Giering, S. Drivers of carbon export efficiency in the Global Ocean. *Glob. Biogeochem. Cycles* **33**, 891–903 (2019).

6. Serra-Pompei, C. et al. Linking plankton size spectra and community composition to carbon export and its efficiency. *Glob. Biogeochem. Cycles* **36**, e2021GB007275 (2022).
7. Sheldon, R. W., Sutcliffe, W. H. Jr. & Paranjape, M. A. Structure of pelagic food chain and relationship between plankton and fish production. *J. Fish. Res. Board Can.* **34**, 2344–2353 (1977).
8. Rykaczewski, R. R. & Checkley, D. M. Influence of ocean winds on the pelagic ecosystem in upwelling regions. *Proc. Natl. Acad. Sci. USA*. **105**, 1965–1970 (2008).
9. Maranón, E., Cermeóo, P., Rodríguez, J., Zubkov, M. V. & Harris, R. P. Scaling of phytoplankton photosynthesis and cell size in the ocean. *Limnol. Oceanogr.* **52**, 2190–2198 (2007).
10. Kiørboe, T. & Hirst, A. G. Shifts in mass scaling of respiration, feeding, and growth rates across life-form transitions in marine pelagic organisms. *Am. Nat.* **183**, E118–E130 (2014).
11. Hansen, B., Bjornsen, P. K. & Hansen, P. J. The size ratio between planktonic predators and their prey. *Limnol. Oceanogr.* **39**, 395–403 (1994).
12. Stamieszkin, K. et al. Size as the master trait in modeled copepod fecal pellet carbon flux. *Limnol. Oceanogr.* **60**, 2090–2107 (2015).
13. Uye, S. & Kaname, K. Relations between fecal pellet volume and body size for major zooplankters of the Inland Sea of Japan. *J. Oceanogr.* **50**, 43–49 (1994).
14. Chindia, J. A. & Figueredo, C. C. Phytoplankton settling depends on cell morphological traits, but what is the best predictor? *Hydrobiologia* **813**, 51–61 (2018).
15. Andersen, K. H. et al. Characteristic sizes of life in the oceans, from bacteria to whales. *Annu. Rev. Mar. Sci.* **8**, 217–241 (2016).
16. Blanchard, J. L., Heneghan, R. F., Everett, J. D., Trebilco, R. & Richardson, A. J. From bacteria to whales: using functional size spectra to model marine ecosystems. *Trends Ecol. Evol.* **32**, 174–186 (2017).
17. Hatton, I. A., Heneghan, R. F., Bar-On, Y. M. & Galbraith, E. D. The global ocean size spectrum from bacteria to whales. *Sci. Adv.* **7**, eabh3732 (2021).
18. Heneghan, R. F., Hatton, I. A. & Galbraith, E. D. Climate change impacts on marine ecosystems through the lens of the size spectrum. *Emerg. Top. Life Sci.* **3**, 233–243 (2019).
19. Pierella Karlusich, J. J. et al. Global distribution patterns of marine nitrogen-fixers by imaging and molecular methods. *Nat. Commun.* **12**, 4160 (2021).
20. Brandão, M. C. et al. Macroscale patterns of oceanic zooplankton composition and size structure. *Sci. Rep.* **11**, 15714 (2021).
21. Barton, A. D. et al. The biogeography of marine plankton traits. *Ecol. Lett.* **16**, 522–534 (2013).
22. Panaïotis, T. et al. Three major mesoplanktonic communities resolved by in situ imaging in the upper 500 m of the global ocean. *Glob. Ecol. Biogeogr.* **32**, 1991–2005 (2023).
23. Atkinson, D. & Sibly, R. M. Why are organisms usually bigger in colder environments? Making sense of a life history puzzle. *Trends Ecol. Evol.* **12**, 235–239 (1997).
24. Brun, P., Payne, M. R. & Kiørboe, T. Trait biogeography of marine copepods – an analysis across scales. *Ecol. Lett.* **19**, 1403–1413 (2016).
25. Wrightson, L. & Tagliabue, A. Quantifying the impact of climate change on marine diazotrophy: insights from Earth system models. *Front. Mar. Sci.* **7**, 635 (2020).
26. Faure, E. et al. Mixotrophic protists display contrasted biogeographies in the global ocean. *ISME J.* **13**, 1072–1083 (2019).
27. Laget, M. et al. Global census of the significance of giant mesopelagic protists to the marine carbon and silicon cycles. *Nat. Commun.* **15**, 3341 (2024).
28. Beck, M. et al. Morphological diversity increases with decreasing resources along a zooplankton time series. *Proc. R. Soc. B Biol. Sci.* **290**, 2109 (2023).
29. Vilgrain, L. et al. Trait-based approach using in situ copepod images reveals contrasting ecological patterns across an Arctic ice melt zone. *Limnol. Oceanogr.* **66**, 1155–1167 (2021).
30. Kiørboe, T., Visser, A. & Andersen, K. H. A trait-based approach to ocean ecology. *ICES J. Mar. Sci.* **75**, 1849–1863 (2018).
31. Litchman, E., Ohman, M. D. & Kiørboe, T. Trait-based approaches to zooplankton communities. *J. Plankton Res.* **35**, 473–484 (2013).
32. Ohman, M. D. & Romagnan, J.-B. Nonlinear effects of body size and optical attenuation on Diel Vertical Migration by zooplankton. *Limnol. Oceanogr.* **61**, 765–770 (2016).
33. Litchman, E., Klausmeier, C. A., Schofield, O. M. & Falkowski, P. G. The role of functional traits and trade-offs in structuring phytoplankton communities: scaling from cellular to ecosystem level. *Ecol. Lett.* **10**, 1170–1181 (2007).
34. Martini, S. et al. Functional trait-based approaches as a common framework for aquatic ecologists. *Limnol. Oceanogr.* **66**, 965–994 (2021).
35. Orenstein, E. C. et al. Machine learning techniques to characterize functional traits of plankton from image data. *Limnol. Oceanogr.* **67**, 1647–1669 (2022).
36. Lombard, F. et al. Globally consistent quantitative observations of planktonic ecosystems. *Front. Mar. Sci.* **6**, 196 (2019).
37. Kiko, R., Lopes, R. M., Soviadan, Y. D. & Stemmann, L. Towards a distributed and operational pelagic imaging network. *Ocean Coast. Res.* **71**, e23058 (2023).
38. Tagliabue, A. et al. The integral role of iron in ocean biogeochemistry. *Nature* **543**, 51–59 (2017).
39. Wang, L.-C. & Jia-Yuh, Y. Dynamics of upwelling annual cycle in the equatorial Pacific Ocean. *Sustainability* **11**, 5038 (2019).
40. Tagliabue, A. et al. A global compilation of dissolved iron measurements: focus on distributions and processes in the Southern Ocean. *Biogeosciences* **9**, 2333–2349 (2012).
41. Benedetti, F., Wydler, J. & Vogt, M. Copepod functional traits and groups show divergent biogeographies in the global ocean. *J. Biogeogr.* **50**, 8–22 (2023).
42. Seibel, B. A., Schneider, J. L., Kaartvedt, S., Wishner, K. F. & Daly, K. L. Hypoxia tolerance and metabolic suppression in oxygen minimum zone euphausiids: implications for ocean deoxygenation and biogeochemical cycles. *Integr. Comp. Biol.* **56**, 510–523 (2016).
43. Kiko, R., Hauss, H., Buchholz, F. & Melzner, F. Ammonium excretion and oxygen respiration of tropical copepods and euphausiids exposed to oxygen minimum zone conditions. *Biogeosciences* **13**, 2241–2255 (2016).
44. Regaudie-de-Gioux, A. & Duarte, C. M. Temperature dependence of planktonic metabolism in the ocean. *Glob. Biogeochem. Cycles* **26**, 1–10 (2012).
45. Staal, M., Meysman, F. J. R. & Stal, L. J. Temperature excludes N2-fixing heterocystous cyanobacteria in the tropical oceans. *Nature* **425**, 504–507 (2003).
46. Stal, L. J. Is the distribution of nitrogen-fixing cyanobacteria in the oceans related to temperature? *Environ. Microbiol.* **11**, 1632–1645 (2009).
47. Inomura, K., Wilson, S. T. & Deutsch, C. Mechanistic model for the coexistence of nitrogen fixation and photosynthesis in marine Trichodesmium. *mSystems* **4**, e00210–e00219 (2019).
48. Lombard, F., Erez, J., Michel, E. & Labeyrie, L. Temperature effect on respiration and photosynthesis of the symbiont-bearing planktonic foraminifera Globigerinoides ruber, Orbulina universa, and Globigerinella siphonifera. *Limnol. Oceanogr.* **54**, 210–218 (2009).
49. Villar, E. et al. Symbiont chloroplasts remain active during bleaching-like response induced by thermal stress in Collozoum pelagicum (Collodaria, Retaria). *Front. Mar. Sci.* **5**, 387 (2018).
50. Daufresne, M., Lengfellner, K. & Sommer, U. Global warming benefits the small in aquatic ecosystems. *Proc. Natl. Acad. Sci. USA*. **106**, 12788–12793 (2009).

51. Rice, E., Dam, H. G. & Stewart, G. Impact of climate change on estuarine zooplankton: surface water warming in Long Island Sound is associated with changes in copepod size and community structure. *Estuaries Coasts* **38**, 13–23 (2015).
52. Heneghan, R. F., Everett, J. D., Blanchard, J. L., Sykes, P. & Richardson, A. J. Climate-driven zooplankton shifts cause large-scale declines in food quality for fish. *Nat. Clim. Change* **13**, 470–477 (2023).
53. Guidi, L. et al. Plankton networks driving carbon export in the oligotrophic ocean. *Nature* **532**, 465–470 (2016).
54. Agusti, S. et al. Ubiquitous healthy diatoms in the deep sea confirm deep carbon injection by the biological pump. *Nat. Commun.* **6**, 7608 (2015).
55. Benavides, M. et al. Sinking Trichodesmium fixes nitrogen in the dark ocean. *ISME J.* **16**, 2398–2405 (2022).
56. Tovar-Sanchez, A. et al. Effects of dust deposition and river discharges on trace metal composition of trichodesmium spp. in the tropical and subtropical North Atlantic Ocean. *Limnol. Oceanogr.* **51**, 1755–1761 (2006).
57. Fernández, A., Mouriño-Carballido, B., Bode, A. & Varela, M. & Marañón, E. Latitudinal distribution of *Trichodesmium* spp. and $N_2$ fixation in the Atlantic Ocean. *Biogeosciences* **7**, 3167–3176 (2010).
58. Langlois, R. J., Mills, M. M., Ridame, C., Croot, P. & LaRoche, J. Diazotrophic bacteria respond to Saharan dust additions. *Mar. Ecol. Prog. Ser.* **470**, 1–14 (2012).
59. Yoon, J.-E., King, D., Longman, J. & Cronin, S. J. Differential response of chlorophyll-a concentrations to explosive volcanism in the western South Pacific. *Front. Mar. Sci.* **10**, 1072610 (2023).
60. Li, M., Shen, F. & Sun, X. 2019–2020 Australian bushfire air particulate pollution and impact on the South Pacific Ocean. *Sci. Rep.* **11**, 12288 (2021).
61. Guieu, C. et al. Iron from a submarine source impacts the productive layer of the Western Tropical South Pacific (WTSP). *Sci. Rep.* **8**, 9075 (2018).
62. Bonnet, S. et al. Natural iron fertilization by shallow hydrothermal sources fuels diazotroph blooms in the ocean. *Science* **380**, 812–817 (2023).
63. Mériguet, Z. et al. Plankton community structure in response to hydrothermal iron inputs along the Tonga-Kermadec arc. *Front. Mar. Sci.* **10**, 1232923 (2023).
64. Liu, J. et al. Historical footprints and future projections of global dust burden from bias-corrected CMIP6 models. *npj Clim. Atmos. Sci.* **7**, 1–12 (2024).
65. Wang, P. et al. Aerosols overtake greenhouse gases causing a warmer climate and more weather extremes toward carbon neutrality. *Nat. Commun.* **14**, 7257 (2023).
66. Gomez, J. et al. The projected future degradation in air quality is caused by more abundant natural aerosols in a warmer world. *Commun. Earth Environ.* **4**, 1–11 (2023).
67. Moore, C. M. et al. Processes and patterns of oceanic nutrient limitation. *Nat. Geosci.* **6**, 701–710 (2013).
68. Laglera, L. M. et al. Iron partitioning during LOHAFEX: copepod grazing as a major driver for iron recycling in the Southern Ocean. *Mar. Chem.* **196**, 148–161 (2017).
69. Tsuda, A. et al. Evidence for the grazing hypothesis: Grazing reduces phytoplankton responses of the HNLC ecosystem to iron enrichment in the Western Subarctic Pacific (SEEDS II). *J. Oceanogr.* **63**, 983–994 (2007).
70. Winkelbauer, S. et al. Diagnostic evaluation of river discharge into the Arctic Ocean and its impact on oceanic volume transports. *Hydrol. Earth Syst. Sci.* **26**, 279–304 (2022).
71. Huang, Y., Tagliabue, A. & Cassar, N. Data-driven modeling of dissolved Iron in the Global Ocean. *Front. Mar. Sci.* **9**, 837183 (2022).
72. Picheral, M. et al. The Underwater Vision Profiler 5: An advanced instrument for high spatial resolution studies of particle size spectra and zooplankton. *Limnol. Oceanogr. Methods* **8**, 462–473 (2010).
73. Picheral, M. et al. The Underwater Vision Profiler 6: an imaging sensor of particle size spectra and plankton, for autonomous and cabled platforms. *Limnol. Oceanogr. Methods* **20**, 115–129 (2022).
74. Gorsky, G. et al. Digital zooplankton image analysis using the ZooScan integrated system. *J. Plankton Res.* **32**, 285–303 (2010).
75. Dugenne, M. et al. First release of the Pelagic Size Structure database: global datasets of marine size spectra obtained from plankton imaging devices. *Earth Syst. Sci. Data Discuss.* 1–41. https://doi.org/10.5194/essd-2023-479 (2023).
76. Kiko, R. et al. A global marine particle size distribution dataset obtained with the Underwater Vision Profiler 5. *Earth Syst. Sci. Data* **14**, 4315–4337 (2022).
77. Neeley, A. et al. Standards and practices for reporting plankton and other particle observations from images. 38pp. https://doi.org/10.1575/1912/27377 (2021).
78. Drago, L. et al. Global distribution of zooplankton biomass estimated by in situ imaging and machine learning. *Front. Mar. Sci.* **9**, 894372 (2022).
79. Boyer, T. P. et al. *World Ocean Atlas 2018*. (NOAA National Centers for Envrionmental Information, 2018).
80. Tagliabue, A. et al. How well do global ocean biogeochemistry models simulate dissolved iron distributions? *Glob. Biogeochem. Cycles* **30**, 149–174 (2016).
81. Gledhill, M. & Buck, K. The organic complexation of iron in the marine environment: a review. *Front. Microbiol.* **3**, 69 (2012).
82. Aumont, O., Ethé, C., Tagliabue, A., Bopp, L. & Gehlen, M. PISCES-v2: an ocean biogeochemical model for carbon and ecosystem studies. *Geosci. Model Dev.* **8**, 2465–2513 (2015).
83. Tanner, E. P., Ewin, H., Viljoen, J. J. & Brewin, R. J. W. Revisiting the relationship between surface and column-integrated chlorophyll-a concentrations in the Biogeochemical-Argo and satellite era. *Front. Remote Sens.* **5**, 1495958 (2024).
84. Silsbe, G. M., Behrenfeld, M. J., Halsey, K. H., Milligan, A. J. & Westberry, T. K. The CAFE model: a net production model for global ocean phytoplankton. *Glob. Biogeochem. Cycles* **30**, 1756–1777 (2016).
85. Kostadinov, T. S. et al. Ocean color algorithm for the retrieval of the particle size distribution and carbon-based phytoplankton size classes using a two-component coated-sphere backscattering model. *Ocean Sci.* **19**, 703–727 (2023).
86. Chelton, D. B., Schlax, M. G. & Samelson, R. M. Global observations of nonlinear mesoscale eddies. *Prog. Oceanogr.* **91**, 167–216 (2011).
87. Elith, J., Leathwick, J. R. & Hastie, T. A working guide to boosted regression trees. *J. Anim. Ecol.* **77**, 802–813 (2008).
88. Steele, R. J. & Raftery, A. E. Performance of Bayesian Model Selection Criteria for Gaussian Mixture Models. Edited by M.-H. Chen et al. in *Frontiers of Statistical Decision Making and Bayesian Analysis* 113–130 (University of Washington Department of Statistics, 2010).


## Author contributions

Conceptualization: M.D., M.C.-U., J.Y.L., R.K., T.O'.B., J.-O.I., F.L., L.S., C.S. Methodology: M.D., M.C.-U., J.Y.L., R.K. Data acquisition: R.K., J.-O.I., F.L., L.S., A.C., L.G., C.G., H.H., A.M.c.D., M.N., M.P. and J.-B.R. Data collection, acquisition, or curation: N.B., S.B., F.C., C.D., L.D., A.E., N.G., J.A.H., L.J., M.L., Z.M., B.N., T.P., E.R., J.T., C.T., M.V. Visualization: M.D. Supervision: J.Y.L., R.K. Writing—original draft: M.D. Writing—review and editing: all authors.

## Funding

This work was primarily funded by NOAA, award NA21OAR4310254 (J.L., R.K., L.S., F.L., J.-O.I., T.O'.B., and C.S.), in addition to the following funding programs: European Union Horizon 2020 program grant 817578 (M.D., R.K., and L.S.), French National Research Agency (ANR), Programme d'Investissements d'Avenir grant #ANR-19-MPGA-0012 (R.K.), and Heisenberg Programme of the German Science Foundation #KI1387/5-1 (R.K.). Open Access funding enabled and organized by Projekt DEAL.

## Competing interests
The authors declare no competing interests.

## Additional information
**Supplementary information** The online version contains supplementary material available at https://doi.org/10.1038/s41467-026-75355-4.

**Correspondence** and requests for materials should be addressed to Mathilde Dugenne or Rainer Kiko.

**Peer review information** *Nature Communications* thanks Alex Poulton and the other, anonymous, reviewer(s) for their contribution to the peer review of this work. A peer review file is available.

**Reprints and permissions information** is available at http://www.nature.com/reprints

**Publisher's note** Springer Nature remains neutral with regard to jurisdictional claims in published maps and institutional affiliations.

**Open Access** This article is licensed under a Creative Commons Attribution 4.0 International License, which permits use, sharing, adaptation, distribution and reproduction in any medium or format, as long as you give appropriate credit to the original author(s) and the source, provide a link to the Creative Commons licence, and indicate if changes were made. The images or other third party material in this article are included in the article's Creative Commons licence, unless indicated otherwise in a credit line to the material. If material is not included in the article's Creative Commons licence and your intended use is not permitted by statutory regulation or exceeds the permitted use, you will need to obtain permission directly from the copyright holder. To view a copy of this licence, visit http://creativecommons.org/licenses/by/4.0/.

© The Author(s) 2026

## PSSdb data contributors

**Marc Picheral[1], Lionel Guidi[1], Andrew M. P. McDonnell[6], Laetitia Drago[1], Zoé Mériguet[1], Marion Vilain[1], Chloé Tilliette[1], Nagib Bhairy[7], Sophie Bonnet[7], Thelma Panaïotis[1], Margaux Noyon[8], Cécile Guieu[1], Astrid Cornils[9], Jean-Baptiste Romagnan[10], Nina Grandrémy[10], François Carlotti[7], Magali Lescot[7], Emilie Riquier[1], Laetitia Jalabert[1], Amanda Elineau[1], Corinne Desnos[1], Helena Hauss[5], Jan Taucher[5], Barbara Niehoff[9] & Jenny Huggett[11]**

[6]Oceanography Department, University of Alaska Fairbanks, Fairbanks, AK, USA. [7]Mediterranean Institute of Oceanography, Marseille, France. [8]Department of Oceanography and Institute for Coastal and Marine Research, Nelson Mandela University, Gqeberha, South Africa. [9]Polar Biological Oceanography, Alfred Wegener Institute Helmholtz Centre for Polar and Marine Research, Bremerhaven, Germany. [10]DECOD, IFREMER, INRAE, Institut Agro, Nantes, France. [11]Oceans and Coastal Research, Department of Forestry, Fisheries and the Environment, Cape Town, South Africa.